THz time-domain spectroscopy modulated with semiconductor plasmonic perfect absorbers

Fernando Gonzalez-Posada, Dominique Coquillat, Melissa Najem, Laurent Cerutti, Thierry Taliercio

▶ **To cite this version:**

Fernando Gonzalez-Posada, Dominique Coquillat, Melissa Najem, Laurent Cerutti, Thierry Taliercio. THz time-domain spectroscopy modulated with semiconductor plasmonic perfect absorbers. Optics Express, 2023, 31 (20), pp.32152. 10.1364/OE.498479 . hal-04282047

HAL Id: hal-04282047
https://hal.science/hal-04282047

Submitted on 13 Nov 2023

HAL is a multi-disciplinary open access archive for the deposit and dissemination of scientific research documents, whether they are published or not. The documents may come from teaching and research institutions in France or abroad, or from public or private research centers.

L'archive ouverte pluridisciplinaire **HAL**, est destinée au dépôt et à la diffusion de documents scientifiques de niveau recherche, publiés ou non, émanant des établissements d'enseignement et de recherche français ou étrangers, des laboratoires publics ou privés.

Research Article Vol. 31, No. 20 / 25 Sep 2023 / Optics Express 32152
Optics EXPRESS

THz time-domain spectroscopy modulated with semiconductor plasmonic perfect absorbers

FERNANDO GONZALEZ-POSADA,[1,*] DOMINIQUE COQUILLAT,[2] MELISSA NAJEM,[1] LAURENT CERUTTI,[1] AND THIERRY TALIERCIO[1]

[1] IES, Université de Montpellier, CNRS, Montpellier, France
[2] Laboratoire Charles Coulomb (L2C), Université de Montpellier, CNRS, Montpellier, France
[*] fernando.gonzalez-posada-flores@umontpellier.fr

Abstract: Terahertz time-domain spectroscopy (THz-TDS) at room temperature and standard atmosphere pressure remains so far the backbone of THz photonics in numerous applications for civil and defense levels. Plasmonic microstructures and metasurfaces are particularly promising for improving THz spectroscopy techniques and developing biomedical and environmental sensors. Highly doped semiconductors are suitable for replacing the traditional plasmonic noble metals in the THz range. We present a perfect absorber structure based on semiconductor III-Sb epitaxial layers. The insulator layer is GaSb while the metal-like layers are Si doped InAsSb ($\sim 5{\cdot}10^{19}\,cm^{-3}$). The doping is optically measured in the IR with polaritonic effects at the Brewster angle mode. Theoretically, the surface can be engineered in frequency selective absorption array areas of an extensive THz region from 1.0 to 6.0 THz. The technological process is based on a single resist layer used as hard mask in dry etching defined by electron beam lithography. A wide 1350 GHz cumulative bandwidth experimental absorption is measured in THz-TDS between 1.0 and 2.5 THz, only limited by the air-exposed reflectance configuration. These results pave the way to implement finely tuned selective surfaces based on semiconductors to enhance light-matter interaction in the THz region.

© 2023 Optica Publishing Group under the terms of the Optica Open Access Publishing Agreement

1. Introduction and motivation

In the last decades, different technologies tend to rely on the world of transistors and lasers in order to fill the terahertz (THz) gap. Some applications target medical diagnosis, industrial processing, environment control at a civil level; and substance analysis, night observation and security countermeasures at a defense level. In this sense, optical instrumentation and devices are required with high resolution, sensitivity and spectral selectivity compatible with the silicon technology. THz spectroscopy is a promising method to measure the spectrum of low-frequency vibrational modes of molecules or ensembles, such as crystals and polymers, including proteins. However, the main drawback of THz spectroscopy is its extremely low sensitivity [1], in contrast to a high signal-to-noise ratio [2]. Plasmonic microstructures and metasurfaces are particularly promising for improving THz spectroscopy techniques and for the development of biomedical and environmental sensors [3–6].

Localized surface plasmon resonances (LSPR) on micro-structured antennas operating at THz frequencies give rise to very large local electromagnetic (EM) field enhancements and subwavelength confinements near the metal structures [7]. These field enhancements are very promising to increase the sensitivity of chemical or biological sensors, similar to the sensing strategies in the visible and the near-infrared (IR) regions [8]. In the far-field, the surface-enhanced THz spectroscopy is characterized by absorption peaks in the extinction spectrum where identification may be based on the spectral fingerprints available, as expected in THz immunobiosensing research [9]. Furthermore, the combination of IR and THz-TDS spectroscopy will exploit both technique advantages in studying material characteristic absorption spectra [10]

#498479 https://doi.org/10.1364/OE.498479
Journal © 2023 Received 21 Jun 2023; revised 31 Aug 2023; accepted 31 Aug 2023; published 12 Sep 2023

Optics EXPRESS

and LSPR antennas can effectively improve them when their properties adjusted to the material finger-print regions.

Metals have been traditionally used for experimental demonstrations in sensing enhancement. For instance, nanoscale slits in a metal screen can produce giant field enhancements [11], which can then improve the ability to detect an analyte of interest [12], using the modulation of the transmitted intensity or the peak shift of absorption resonances [13]. Recently, THz imaging with metamaterials for biological applications used metallic split ring resonators to enhanced human embryonic kidney cells [14], and for polymerase chain reaction free cDNA detection based on frequency selective surfaces with a substrate-integrated microfluidic THz biosensor [15–17].

Semiconductors are promising candidates for active plasmonic devices at THz frequencies. Semiconductors have a Drude-like behavior at THz frequencies similar to metals at optical frequencies. Narrow band gap semiconductors like Si [18], GaAs [19], InSb [20], InAs [21] have a dielectric function with a negative real component and a relatively small imaginary component. This permittivity is characteristic of noble metals in the visible. Therefore, similar to metals at optical frequencies, semiconductors sustain surface plasmon polaritons (SPPs) or collective oscillations of free charge carriers at the interface with a dielectric [22].

Our previous works demonstrate that highly doped semiconductors are suitable for replacing the traditionally-used noble metals [23]. The permittivity of these semiconductors is more than one order of magnitude lower than traditional metals. Semiconductors antennas have stronger EM-field confinements owing to their much lower free carrier concentration compared to metals. The plasmonic antenna behaviors are optically tuned with different geometry, size and interactions (gap effect) in the IR [24] and THz range [25]. Most importantly, the doping gives an additional degree of freedom to actively control the LSPRs and the enhanced field interacts with the perfect absorber structure mimicking a simple metal-insulator-metal (MIM) with an optimized GaSb spacer [26]. In this sense, the concept of perfect metamaterial absorbers takes advantage of the intrinsic semiconductor structure losses. Basically, the idea is to minimize the reflectance through impedance matching and simultaneously eliminate the transmittance by maximizing the metamaterial losses [27].

In this work, perfect absorbers with III-V semiconductors are presented as modulators of the EM spectra in the THz range between 1.0 and 6.0 THz. These perfect absorbers are based on a thick dielectric layer in comparison to our previous results in perfect absorbers in order to originate localized surface plasmon resonances in the THz range independent of the photonic mode of the absorber cavity. In the THz region, a discretization of the EM spectrum is achieved with a clear absorption modulation corresponding to the frequency selective surface engineering. This work paves the way on how to manipulate THz light and use semiconductors as support for sensing applications in the THz spectrometers.

2. Experimental section

Samples were grown with molecular beam epitaxy on a Te n-doped 2-inch GaSb substrate. First, a 200 nm GaSb buffer layer was grown to activate the surface and bury possible native mismatch-induced defects. Then the perfect absorber layers are grown. The perfect absorber is composed of three layers from bottom to top: (i) a 995 nm thick InAsSb layer highly n-doped at nominally $4.2{\cdot}10^{19}\,\mathrm{cm}^{-3}$, (ii) a 2 µm non-intentionally doped GaSb spacer and (iii) a 200 nm InAsSb layer highly n-doped at nominally $4.2{\cdot}10^{19}\,\mathrm{cm}^{-3}$. Silicon was used for n-type doping within $InAs_{0.91}Sb_{0.09}$ in its lattice-matched exact composition configuration for an optimal low-defect epitaxial growth. The spacer layer is thick enough in order to achieve plasmonic resonances in the THz range with a microstructured surface, as introduced by F. Omeis *et al.* [25]. X-ray diffraction measurements confirms the nominal thickness and alloy concentrations.

THz time-domain spectroscopy (THz-TDS) measurements are done on a commercial THz system (TeraPulse 4000 TeraView Ltd., Cambridge, UK) in reflectance configuration. THz

Optics EXPRESS

radiation is produced by ultra-short pulse fiber laser (pulse duration <100 fs). One portion of the beam is focused onto a photoconductive antenna which is used to generate the THz radiation. The other portion of the beam is used as a 'time-gating' probe to detect the THz radiation using a second photoconductive antenna. Parabolic mirrors focus the THz radiation onto the sample in reflectance mode. The incident light is perpendicular to the sample surface and linearly polarized. More details about THz technology can be found in Jepsen *et al.* [28]. Measurements were performed in rapid scan mode at a rate of 15 scans/second, providing a useful spectral range 0.2–3.0 THz (6–100 cm^{-1}) with an optical delay extend of 35 ps, enabling a high spectral resolution of ~30 GHz. Spectra were the average of 50 scans. The sample section is nitrogen-purged to make sure that no residual water vapor peaks are visible in the spectra. The samples under investigation were directly placed on the sample holder which is an aluminum disk with a 2 cm diameter hole at the center. The sample region of interest is maintained steady in an average plane. Concerning the structure, the upper epitaxial layer was facing the incoming THz pulse. The whole surface images are $\sim 8 \times 15$ mm. The pixel scans were done in steps of 0.1 mm in both directions for each spectrum. A gold reference is used at the beginning of the experiment for the intensity calibration set-up. For the reflectance spectra, the flat sample surface is used as reference.

Rigorous coupled wavelength analysis (RCWA) is used to calculate the absorption, reflection and transmission based on J-P. Hugonin and P. Lalane open-acess code RETICOLO supported by Matlab [29]. Periodic boundary conditions are used to mimic periodic structures. For computation with high accuracy the Fourier harmonics retained was set to 40, after convergence tests with higher values. A Drude model with the phonons influence was used to find the material parameters based on the following equation:

$$\varepsilon(\omega) = \varepsilon_\infty \cdot \left(1 - \frac{\omega_p^2}{\omega_p^2 + i\gamma\omega} + \frac{\omega_{LO}^2 - \omega^2 - i\Gamma\omega}{\omega_{TO}^2 - \omega^2 - i\Gamma\omega}\right); \qquad \omega_p^2 = \frac{Ne^2}{\varepsilon_0 \varepsilon_\infty m^*} \tag{1}$$

where ε_∞ is the high-frequency permittivity, ω_p is the plasma frequency in rad·s^{-1}, γ is the electronic damping parameter in rad·s^{-1}, ω_{LO} is the longitudinal optical phonon in rad·s^{-1}, ω_{TO} is the transversal optical phonon in rad·s^{-1}, Γ is the phonon damping parameter in rad·s^{-1}, N the density of free carriers (i.e., the doping level) in cm^{-3}, ε_0 is the vacuum permittivity and m^* the effective mass. In Table 1, InAsSb and GaSb values used for the simulation are summarized for clarity:

Table 1. Material parameters for InAsSb and GaSb used in the RCWA simulation to implement the Drude model taking into account the phonon resonances in the periodic structures [24,26]

	ε_∞	γ (rad·s^{-1})	ω_{LO} (rad·s^{-1})	ω_{TO} (rad·s^{-1})	Γ (rad·s^{-1})
InAsSb	10.4	10^{13}	$4.40 \cdot 10^{13}$	$4.04 \cdot 10^{13}$	$5.6 \cdot 10^{11}$
GaSb	14.4	-	$4.39 \cdot 10^{13}$	$4.22 \cdot 10^{13}$	$5.6 \cdot 10^{11}$

The fabrication process is done in a cleanroom environment. Sample surface is cleaned with acetone, followed by isopropanol each for 2 min and dry with blown N_2. Then, the samples are dehydrated at 110°C for 2 min. A diluted AZ2020:AZEBR (100:80) negative resist is deposited by spin coating (6000 rpm for 30 s, with a 2 s ramp acceleration) and baked at 110°C for 1 min. The microstructures were defined by e-beam lithography (EBL from Raith GmbH nanofabrication coupled to a SEM from JEOL) with a nominal dose of 14.67 μC/cm^2 achieved with a beam current of ~ 20 pA, in a 100×100 μm^2 write-field configuration with a 400 times magnification. After lithography, the resist is cross-linked in a post-bake exposure at 110°C for 1 min and developed for 30 s using AZ726 MIF developer. The InAsSb top layer is etched using an Ar-based plasma inductively coupled plasma etching (ICP-RIE from Oxford Instruments PLC)

Optics EXPRESS

with 25 sccm Ar, 5 Torr, RF power: 50 W, ICP generator power: 500 W, at 60 °C, with 5 sccm He for 10 min. The final surface cleaning with acetone, followed by isopropanol each for 2 min and dry with blown N_2, ends with a plasma oxygen for 2 min. (100 sccm, 0.7 mbar).

3. Results and discussion

The III-V semiconductor perfect absorber consists in three distinct layers (Fig. 1(a)). After the sample epitaxial growth, the doping of the metallic-like InAsSb layer is verified with an IR optical measurement [30]. The reflectance measurements at an angle of incidence of ~ 60° excite a polaritonic effect: the Brewster mode. The technique is based in the Fresnel formulas coming from the Maxwell macroscopic equations. The Brewster angle (θ_B) is an angle of incidence where reflected light is almost extinguished when the incident light is polarized parallel to the incident plane (TM-mode), see Fig. 1(a). This configuration provides an easy way to extract the plasma frequency, which is correlated to the carrier concentration in Eq. (1).

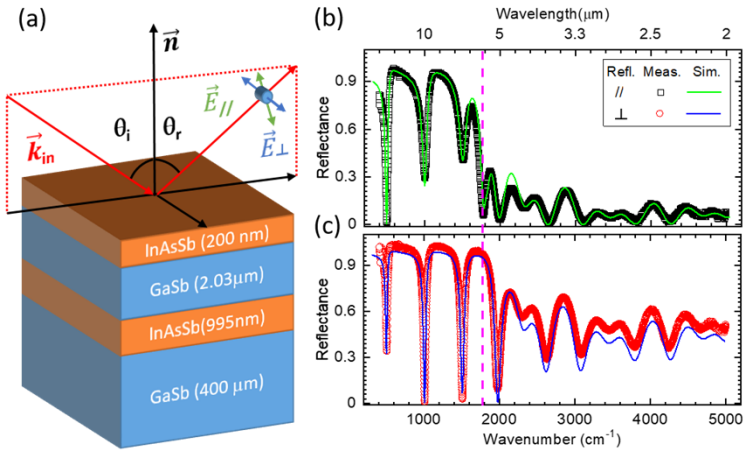

Fig. 1. (a) 3D Layer stacking design of the III-V semiconductor perfect absorber with the FTIR Brewster-mode configuration measurement. IR reflectance measurements near the Brewster angle configuration, $\theta_B \sim 60°$ for an electric field orientation in the measurements done under (b) parallel (TM-mode) and (c) perpendicular (TE-mode) polarizations with respect to the incidence plane defined by the incident wave vector $\vec{k}_{in}$ and the surface normal $\vec{n}$, where θ_i and θ_r are the corresponding incident and reflected angles. The full lines correspond to simulations using transfer matrix method with the corresponding layer thickness, a plasma frequency of 5.6 µm (1773cm^{-1}) and a damping coefficient of $1.2{\cdot}10^{13}$ rad·s^{-1}. The corresponding doping assignment for the InAsSb metal-like layers is $4.65{\cdot}10^{19}$ cm^{-3}. The vertical dashed line indicates the plasma frequency position where reflected parallel light is almost extinguished.

The experimental and simulated reflectance's under parallel (TM-mode) and perpendicular (TE-mode) polarization are presented in Fig. 1(b) and Fig. 1(c), respectively. The reflectance spectra in both polarization measurements present the same absorption deeps corresponding to the perfect absorber structure. However, in the TM-mode the electrical field is parallel, $\vec{E}_{//}$, to the normal incidence plane vector, $\vec{n}$, and when the incidence angle, θ_i, is placed near the Brewster angle position ($\theta_B \sim 60°$), a deep around 1800cm^{-1} (~ 5.5 µm) appears in the reflectance (vertical dashed line). As can be measured in Fig. 1(b) and 1(c), the reflectance amplitude changes radically to ~ 0.06, when light is polarized in the TM-mode (parallel polarization to the incident plane), in contrast to an almost constant value around ~ 0.97, when light is in the TE-mode (perpendicular polarization to the incident plane).

Optics EXPRESS

The simulations based on transfer matrix method adjust the reflection in TM and TE mode considering the nominal epitaxial layer values in Fig. 1(a). From these simulations, the InAsSb metal-like doping results in $4.6{\cdot}10^{19}$ cm^{-3} which corresponds to a plasma frequency of 5.6 µm (1773cm^{-1}) in coherence with previous results by Taliercio *et al.* in InAs layers [30].

After the IR optical characterization, the first metal-like layer of InAsSb was engineered in a clean-room environment. Figure 2(a) shows a visible light diffraction photograph of the partial view of the surface after the technological process with 10 squares. Each square of 1×1 mm^2 contains a grating array of identical linear microstructures with a width, w, ranging from 2 to 28 µm. All the grating periods are the same and correspond to $\Lambda = 30$ µm. Figure 2(b) and 2(c) show scanning electron microscope images of the complete squares of $w = 12$ µm and $w = 28$ µm, respectively. The insets correspond to a partial view of each square engineered surface, to visualize the smooth surface and clear separation resolution. Both images evidence the linearity of the line arrays and the high control of the line array geometries. Figure 2(d) describes a technological process based on a single resist layer used for the definition of the hard mask used in the dry etching defined by electron beam lithography [31]. This process can be adapted to laser lithography, optical lithography or micro-imprint to accelerated and increase the number of THz surface modulators fabricated in a single clean-room process and be cost-effective in mass-production.

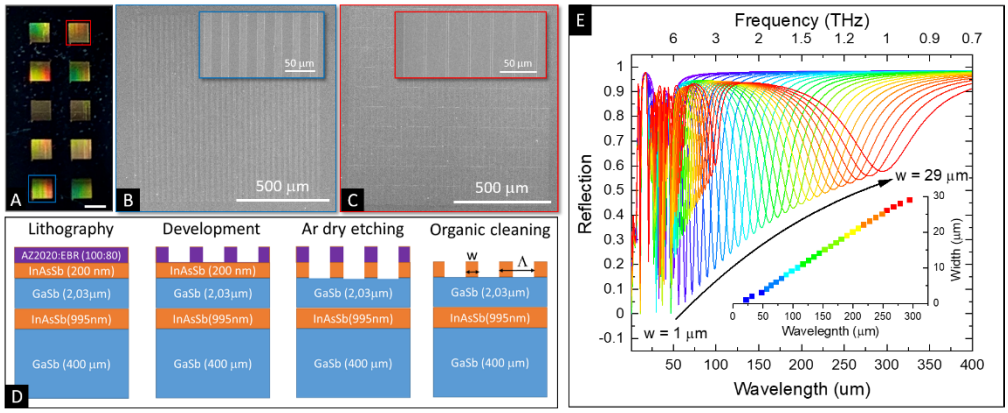

Fig. 2. (a) Photograph of a partial view of the sample surface engineered in the clean-room with 10 squares of 1×1 mm^2 with line arrays of a 30 µm constant period and a variable width from 2 to 28 µm. Scanning electron microscope image (inset) of the whole (partial) square for a line array width of (b) 12 µm and (c) 28 µm. (d) Surface engineering with a 4 step technological process based on a single resist layer for the electron-beam lithography and the dry etching. The structures are defined by the width, w, and their period, Λ, which is constant for the whole sample surface engineered. (e) Simulations of the reflection on the nanoengineered surface for widths from 1 to 29 µm with RCWA. The incident light is perpendicular to the sample surface and linearly polarized perpendicular to the long-axis of the line-arrays. The inset shows the linear dependency of the main plasmonic resonance wavelength with the width geometry.

The perfect absorber structure is designed to absorb in the THz range. The spacer thickness corresponds to a minimization of the reflection through impedance matching from 50 to 300 µm (6 to 1 THz) as shown in Fig. 2(e). Each minima corresponds to a specific line width of the InAsSb top layer nanoengineered in microstructure line-arrays. The effects under THz light illumination are clearly visible as shown in Fig. 3. The C-scan images represent the maximum of the electric field probe in all the points of the surface used in the THz-TDS experimental set-up at a certain time or frequency. In Fig. 3, the C-scan image from the complete samples surface is

Optics EXPRESS

shown for selected frequencies between 0.88 and 2.35 THz. Each image has a different contrast value corresponding to the maximum peak amplitude in the reflected signal. As the frequencies increase in the THz region with $f > 1$ THz, the surface-engineered perfect absorber transductor modulates the THz light dynamically corresponding to the width of the line gratings for each square in the sample surface.

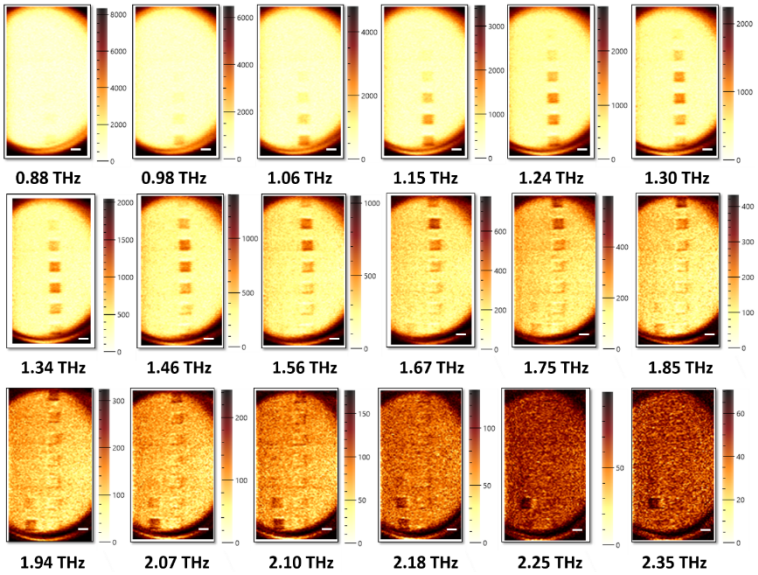

Fig. 3. THz C-scan image in time domain based on the raw data. The contrast mechanism chosen is the maximum peak amplitude in the reflected signal. The light is polarized perpendicular to the microstructured long axis of the line-arrays on the surface. Bar scale for all images is 1 mm. (See Visualization 1 for a high quality image animated video.)

These modulations are a direct consequence of the plasmonic peak shift of the engineered surface into the THz range as the frequency (wavelength) increases (decreases) in agreement with previous plasmonics effects in similar semiconductors grating surfaces [24,26]. In smaller parts of the THz region, similar frequency selective surface based results are also shown with semiconductor III-N gratings [32], with aluminum spiral bull's eye [33], with gold complement split resonators [17], with doped silicon bowties antennas [34] and with perfect absorbers metamaterials based in aluminum [35] or gold [27]. In comparison, the absorption bandwidth modulated is wide, ~1350 GHz, by the frequency selective engineered surface based in III-V semiconductors. Note, the frequency selectivity can be retuned and fine-tuned only using the basic geometry characteristics of the engineered array on the surface. The absorption modulation is limited for $f > 3$ THz by the low signal-to-noise of the room temperature conditions under nitrogen flux in the THz-TDS experiment due to water absorption.

To analyze closely the absorption modulation of the perfect absorber in the THz range a Fourier transform is done on the electrical field measurements in the time domain. Then, the reflectance is calculated in single points at the center of each square, dividing the electric field by a reference point in the middle of the sample surface without the top engineered layer into gratings, but with the insulator and the mirror layers. Figure 4(a) shows the reflectance calculated for the width gratings from 12 to 28 μm corresponding to maximum absorption frequencies from 1.17 to 2.40 THz, respectively. We observe the presence of strong noise at high frequencies ($f > 2.5$ THz), for this reason a 9 points average signal on the same width square surface is calculated for Fig. 4(b). Although, the signal-to-noise ratio is reduced, note the maximum electric field has lost

Optics EXPRESS

2 orders of magnitude when $f > 2$ THz in comparison to the $f = 1$ THz, as can be seen in the C-scan images in Fig. 3.

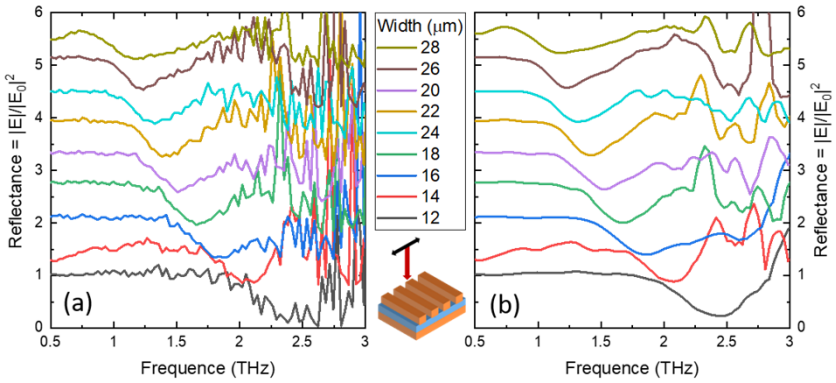

Fig. 4. Reflectance calculated from the electrical field after a Fourier transform of the THz-TDS measurements in the frequency domain (a) for a single pixel center point (b) averaged for 9 different points in the C-scan of each square with different width (w). Note spectra for each width are vertically displaced for better visualization. The inset shows a sketch of the THz light (red arrow) in normal incidence to the surface with a linear polarization (black double-arrow) perpendicular to the line-arrays long axis.

A peak fit is used to obtain the centroid position, the absorption intensity and the full-width half-maximum (FWHM) of all the grating square average reflectance in Fig. 4. These values are represented in Fig. 5(a) (red dots with labels of the absorption maximum frequency in THz) on top of an absorption cartography map (z-axis) in function of the engineered grating width (y-axis) and the wavelength position in μm (x-axis). Simulations are done by RCWA [29]. The plasmonic peak corresponding to the engineered grating on the top surface shows a linear dependency with the wavelength from $\lambda > 50$ μm. Below this wavelength, the evidence of the strong coupling regime between plasmonic resonances with the phonons at lower wavelengths (25–50 μm) measured by FTIR is confirmed [36].

The wavelength (i.e., frequency) position calculated from the simulations shows a similar linear dependency with the engineered square grating widths as the maximum absorption positions measured in the THz-TDS Fourier transform reflectance calculated in Fig. 4(b). Figure 5(b) correlates this linear dependency with the intensity of the absorption measured and simulated. This proportionality states an effective refractive index of ~ 5 for the MIM structure, taking into account a simple vibrating cord model for the first mode. A clear difference between the simulated and measured mainly due to the difference in the parameters used for the simulation in terms of losses (gamma) and technological geometry differences after the fabrication. For $w = 12$ μm and 28 μm, the absorption is over- and under- estimated, respectively, due to the error introduced by the high signal-to-noise ratio level from f > 3 THz and the proximity of the THz-TDS set-up aluminum holder, respectively.

Finally, the q-factor of the absorption resonances is calculated as the ratio of the frequency by the full-width half maximum of the absorption resonances. In Fig. 5(c) the THz-TDS measurements show a similar tendency as the RCWA simulations. Note, the RCWA simulations take into account the losses in the microstructured InAs layer. As the width of the line-arrays is wider the wavelength increases (i.e., the frequency decreases) and in all cases the FWHM is wider reducing the q-factor of the microstructured surfaces.

A reduced q-factor with a large FWHM may be beneficial for enhanced sensing applications in the THz regime, where low scattering cross-section absorption frequencies of intermolecular weak forces (such as hydrogen bonds and van der Waals' forces), molecular structure bending,

Optics EXPRESS

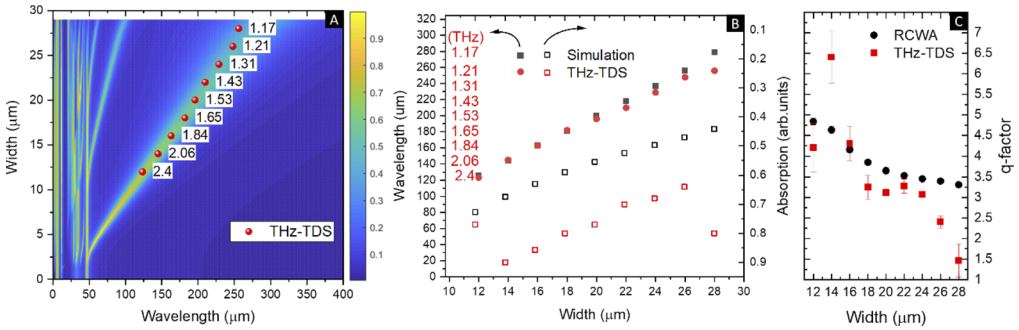

Fig. 5. RCWA simulations and THz-TDS measurement comparison. (a) RCWA absorption map in function of the engineered grating width and the wavelength. Red dots are the absorption maximum frequency position in THz from a Gaussian fit of the reflectance spectra for each grating square from 12 to 28 µm. (b) Simulation and THz-TDS measurements of the maximum absorption wavelength position (red y-scale in THz) and intensity. (c) q-factor evolution with the line-array's width extracted from the RCWA simulations and the THz-TDs measurements.

dipole vibrations and rotational energy transitions as well as low frequency vibrations are mainly located; in contrast to the vibrational absorption frequencies of intramolecular chemical bonds located in the IR band [2]. Indeed, the line-arrays may couple to the molecule systems, resulting in typical spectral features with Fano-like lineshapes of enhanced spectroscopy [8].

4. Conclusion and perspectives

We present a perfect absorber structure based on semiconductor III-Sb epitaxial layers for THz time-domain spectroscopy (THz-TDS). The metal-like layers are doped InAsSb where the doping level is verified by an IR optical measurement based on Brewster angle mode measurements. The frequency selective absorption areas are engineered arrays on the semiconductor surface. The technological process is based on a single resist layer used as a hard mask for dry etching and is scalable to different lithography techniques. The simulated maximum absorption frequency shows a linear correspondence with the array geometry variation in rigorous coupled wave analysis from 1.0 to 6.0 THz. THz-TDS at room temperature and atmospheric pressure reveals the frequency selective areas from 1 to 2.5 THz. The electric field in C-scan is modulated by at least a three-orders of magnitude. The global surface modulation measured with the simple semiconductor arrays expands widely up to ~1350 GHz, and can be finely tuned with the geometry of the perfect absorber top layer. In sum, highly doped III-Sb semiconductors are suitable for implementing in the THz range plasmonic effects tuned with different their geometry as done with current noble metals. Plasmonic modulators based on semiconductors have a strong potential for digital communications, high-performance microwave photonics applications and the development of biomedical and environmental sensing.

Funding. Montpellier Université d'Excellence (PRIME - ENVIRODISORDERS); Région Occitanie Pyrénées-Méditerranée (ESR_PREMAT - 00238); Agence Nationale de la Recherche (ANR-11-EQPX-0016, EXTRA).

Acknowledgments. This work is partially supported by: EXTRA (ANR-11-EQPX-0016), ESR_PREMAT - 00238 / Prématuration 2019 SEA, Region Occitanie and by the Montpellier University of Excellence I-Site MUSE (PRIME - ENVIRODISORDERS). We acknowledge Mrs. Manel HEDHLY ab-initio calculations for the perfect absorbers during her internship. The authors thank clean room technological support from Frédéric Pichot, Jean-Marie Peris, and Renaud Félix. We acknowledge technical support from Guilhem Boissier, Jean-Marc Aniel, Delphine Jourdain, and Ariane Meguekam.

Disclosures. The authors state that they have no conflicts to disclose.

Optics EXPRESS

Data availability. Data underlying the results presented in this paper are not publicly available at this time but may be obtained from the authors upon reasonable request.

References

1. K. Ueno, S. Nozawa, and H. Misawa, "Surface-enhanced terahertz spectroscopy using gold rod structures resonant with terahertz waves," Opt. Express **23**(22), 28584–28592 (2015).
2. C. Song, W.-H. Fan, L. Ding, X. Chen, Z.-Y. Chen, and K. Wang, "Terahertz and infrared characteristic absorption spectra of aqueous glucose and fructose solutions," Sci. Rep. **8**(1), 8964 (2018).
3. D. M. Mittleman, "Frontiers in terahertz sources and plasmonics," Nature Photon **7**(9), 666–669 (2013).
4. S. Adak and L. N. Tripathi, "Nanoantenna Enhanced Terahertz Interaction of Biomolecules," Analyst **144**(21), 6172–6192 (2019).
5. R. Zhou, C. Wang, W. Xu, and L. Xie, "Biological applications of terahertz technology based on nanomaterials and nanostructures," Nanoscale **11**(8), 3445–3457 (2019).
6. J.-H. Kang, D.-S. Kim, and M. Seo, "Terahertz wave interaction with metallic nanostructures," Nanophotonics **7**(5), 763–793 (2018).
7. V. Aglieri, X. Jin, A. Rovere, R. Piccoli, D. Caraffini, S. Tuccio, F. D. Angelis, R. Morandotti, R. Macaluso, A. Toma, and L. Razzari, "Improving nanoscale terahertz field localization by means of sharply tapered resonant nanoantennas," Nanophotonics **9**(3), 683–690 (2020).
8. F. Neubrech, C. Huck, K. Weber, A. Pucci, and H. Giessen, "Surface-Enhanced Infrared Spectroscopy Using Resonant Nanoantennas," Chem. Rev. **117**(7), 5110–5145 (2017).
9. A. Ahmadivand, B. Gerislioglu, R. Ahuja, and Y. Kumar Mishra, "Terahertz plasmonics: The rise of toroidal metadevices towards immunobiosensings," Mater. Today **32**, 108–130 (2020).
10. P. Y. Han, M. Tani, M. Usami, S. Kono, R. Kersting, and X.-C. Zhang, "A direct comparison between terahertz time-domain spectroscopy and far-infrared Fourier transform spectroscopy," J. Appl. Phys. **89**(4), 2357–2359 (2001).
11. M. A. Seo, H. R. Park, S. M. Koo, D. J. Park, J. H. Kang, O. K. Suwal, S. S. Choi, P. C. M. Planken, G. S. Park, N. K. Park, Q. H. Park, and D. S. Kim, "Terahertz field enhancement by a metallic nano slit operating beyond the skin-depth limit," Nat. Photonics **3**(3), 152–156 (2009).
12. H.-R. Park, K. J. Ahn, S. Han, Y.-M. Bahk, N. Park, and D.-S. Kim, "Colossal Absorption of Molecules Inside Single Terahertz Nanoantennas," Nano Lett. **13**(4), 1782–1786 (2013).
13. S. J. Park, J. T. Hong, S. J. Choi, H. S. Kim, W. K. Park, S. T. Han, J. Y. Park, S. Lee, D. S. Kim, and Y. H. Ahn, "Detection of microorganisms using terahertz metamaterials," Sci. Rep. **4**(1), 4988 (2014).
14. Y. Roh, S.-H. Lee, J. Kwak, H. S. Song, S. Shin, Y. K. Kim, J. W. Wu, B.-K. Ju, B. Kang, and M. Seo, "Terahertz imaging with metamaterials for biological applications," Sens. Actuators, B **352**, 130993 (2022).
15. C. Weisenstein, D. Schaar, A. K. Wigger, H. Schäfer-Eberwein, A. K. Bosserhoff, and P. H. Bolívar, "Ultrasensitive THz biosensor for PCR-free cDNA detection based on frequency selective surfaces," Biomed. Opt. Express **11**(1), 448–460 (2020).
16. C. Debus and P. H. Bolivar, "Frequency selective surfaces for high sensitivity terahertz sensing," Appl. Phys. Lett. **91**(18), 184102 (2007).
17. C. Weisenstein, M. Richter, A. K. Wigger, A. Bosserhoff, and P. Haring Bolívar, "Substrate-integrated microfluidics for sensitive biosensing with complementary THz metamaterials in water," Appl. Phys. Lett. **120**(5), 053702 (2022).
18. J. Gómez Rivas, J. Saxler, M. Kuttge, P. Haring Bolívar, and H. Kurz, "Terahertz time-domain spectroscopy of surface plasmon polaritons on semiconductor surfaces," in *Ultrafast Phenomena XIV*, T. Kobayashi, T. Okada, T. Kobayashi, K. A. Nelson, and S. De Silvestri, eds., Springer Series in Chemical Physics (Springer, 2005), pp. 741–743.
19. J. Chochol, K. Postava, M. Čada, M. Vanwolleghem, M. Mičica, L. Halagačka, J.-F. Lampin, and J. Pištora, "Plasmonic behavior of III-V semiconductors in far-infrared and terahertz range," J. Eur. Opt. Soc.-Rapid Publ. **13**(1), 13 (2017).
20. J. G. Rivas and A. Berrier, "Terahertz plasmonics with semiconductor surfaces and antennas," in *Asia Pacific Microwave Conference* (2009), pp. 1293–1296.
21. Y. Zhong, S. D. Malagari, T. Hamilton, and D. Wasserman, "Review of mid-infrared plasmonic materials," J. Nanophotonics **9**(1), 093791 (2015).
22. J. G. Rivas, M. Kuttge, P. H. Bolivar, H. Kurz, and J. A. Sánchez-Gil, "Propagation of Surface Plasmon Polaritons on Semiconductor Gratings," Phys. Rev. Lett. **93**(25), 256804 (2004).
23. F. B. Barho, F. Gonzalez-Posada, M.-J. Milla-Rodrigo, M. Bomers, L. Cerutti, and T. Taliercio, "All-semiconductor plasmonic gratings for biosensing applications in the mid-infrared spectral range," Opt. Express **24**(14), 16175 (2016).
24. M. J. Milla, F. Barho, F. González-Posada, L. Cerutti, M. Bomers, J.-B. Rodriguez, E. Tournié, and T. Taliercio, "Localized surface plasmon resonance frequency tuning in highly doped InAsSb/GaSb one-dimensional nanostructures," Nanotechnology **27**(42), 425201 (2016).
25. F. Omeis, R. Smaali, F. Gonzalez-Posada, L. Cerutti, T. Taliercio, and E. Centeno, "Metal-insulator-metal antennas in the far-infrared range based on highly doped InAsSb," Appl. Phys. Lett. **111**(12), 121108 (2017).
26. F. B. Barho, F. Gonzalez-Posada, L. Cerutti, and T. Taliercio, "Heavily Doped Semiconductor Metamaterials for Mid-Infrared Multispectral Perfect Absorption and Thermal Emission," Adv. Optical Mater. **8**(6), 1901502 (2020).

Optics EXPRESS

27. N. Liu, M. Mesch, T. Weiss, M. Hentschel, and H. Giessen, "Infrared Perfect Absorber and Its Application As Plasmonic Sensor," Nano Lett. **10**(7), 2342–2348 (2010).
28. P. U. Jepsen, D. G. Cooke, and M. Koch, "Terahertz spectroscopy and imaging - Modern techniques and applications: THz spectroscopy and imaging - Modern techniques and applications," Laser & Photon. Rev. **5**(1), 124–166 (2011).
29. J.-P. Hugonin and P. Lalanne, "Light-in-complex-nanostructures/RETICOLO: V9" (2021).
30. T. Taliercio, V. N. Guilengui, L. Cerutti, E. Tournié, and J.-J. Greffet, "Brewster "mode" in highly doped semiconductor layers: an all-optical technique to monitor doping concentration," Opt. Express **22**(20), 24294 (2014).
31. E. Herth, P. Tilmant, M. Faucher, M. François, C. Boyaval, F. Vaurette, Y. Deblocq, B. Legrand, and L. Buchaillot, "Electron beam nanolithography in AZnLOF 2020," Microelectron. Eng. **87**(11), 2057–2060 (2010).
32. V. V. Korotyeyev, Y. M. Lyaschuk, V. A. Kochelap, L. Varani, D. Coquillat, S. Danylyuk, S. Brose, and S. A. Vitusevich, "Interaction of sub-terahertz radiation with low-doped grating-based AlGaN/GaN plasmonic structures. Time-domain spectroscopy measurements and electrodynamic modeling," Fiz. Napivprovidn., Kvantova Optoelektron. (1998) **22**(2), 237–251 (2019).
33. X. Deng, L. Li, M. Enomoto, and Y. Kawano, "Continuously Frequency-Tuneable Plasmonic Structures for Terahertz Bio-sensing and Spectroscopy," Sci. Rep. **9**(1), 3498 (2019).
34. A. Berrier, R. Ulbricht, M. Bonn, and J. G. Rivas, "Ultrafast active control of localized surface plasmon resonances in silicon bowtie antennas," Opt. Express **18**(22), 23226–23235 (2010).
35. R. Yahiaoui, S. Tan, L. Cong, R. Singh, F. Yan, and W. Zhang, "Multispectral terahertz sensing with highly flexible ultrathin metamaterial absorber," J. Appl. Phys. **118**(8), 083103 (2015).
36. R. Smaali, F. Omeis, E. Centeno, T. Taliercio, F. Gonzalez-Posada, and L. Cerutti, "Giant Rabi splitting at the phonon line within all-semiconductor metallic-insulator-metallic antennas," Phys. Rev. B **100**(4), 041302 (2019).

162.38.135.106 {ts '2023-11-13 05:58:49'}